Supplementary Information

for

Proton conductivity and magnetization photoswitching in CN-bridged $Cu^{II}_3M^{IV}_2$ molecules (M = Mo, W) based on carboxy-functionalized macrocyclic ligand

Mateusz Reczyński,[a,*] Michał Magott,[a] and Maciej Pazera[a]

[a] Faculty of Chemistry, Jagiellonian University in Kraków, Gronostajowa 2, 30-387 Kraków, Poland.

*E-mail: mateusz.reczynski@uj.edu.pl

Experimental details

Materials. All of the reagents necessary to obtain precursors for the following synthesis were purchased from available vendors (Merck, Idalia). The macrocyclic complex α-[Cu(cyclam(COOH)$_2$)](ClO$_4$)$_2$ was obtained based on literature procedures with minor modifications and fully characterized before use (Figures S1-S2).[1, 2] The octacyanidometallates, K$_4$[Mo^{IV}(CN)$_8$]·2H$_2$O[3] and K$_4$[W^{IV}(CN)$_8$]·2H$_2$O,[4] were synthesized according to the literature procedures.

Synthesis and characterization of α-[Cu(cyclam(COOH)$_2$)](ClO$_4$)$_2$

The α-[Cu(cyclam(COOH)$_2$)](ClO$_4$)$_2$ complex was synthesized following the published rout in the three-step process starting from Mannich condensation on the Cu(II) template.[2, 5] The obtained intermediate product of the tetraethyl ester, [Cu(cyclam(COOEt)$_4$)](ClO$_4$)$_2$ (cyclam(COOEt)$_4$ = tetraethyl 1,4,8,11-tetrazacyclotetradecane-6,6,13,13-tetracarboxylate) was hydrolyzed in alkaline conditions to obtain [Cu(cyclam(COOH)$_4$)](ClO$_4$)$_2$·4H$_2$O (cyclam(COOH)$_4$ = 1,4,8,11-tetrazacyclotetradecane-6,6,13,13-tetracarboxylic acid), as we described elsewhere.[6]

α-[Cu(cyclam(COOH)$_2$)](ClO$_4$)$_2$. Solid [Cu(cyclam(COOH)$_4$)](ClO$_4$)$_2$·4H$_2$O (1.41 g, 1.98 mmol) was dissolved in a hot 0.1 M HClO$_4$ solution (20 mL) and refluxed for 90 min. Over this period, the reaction mixture turns deep purple. The solution was cooled down and concentrated HClO$_4$ (5 ml, 70% w/w) was added. The mixture turns red and the crystals of the product form. To complete precipitation, the mixture was refrigerated overnight (−19 °C). The solid product was filtrated, washed with small portions of cold water and ethanol, and air-dried. Yield: 0.859 g (79%). EA. Calculated for C$_{12}$H$_{24}$Cl$_2$CuN$_4$O$_{12}$: C 26.17, H 4.39, N 10:17. Found: C 26.55, H 4.29, N 10.28. *M* = 550.8 g mol^{-1}. IR (cm^{-1}). *ν*(ClO) 996s, 1033s, 1064vs, 1117vs; *ν*(C=O) 1714s; *ν*(C-H) 2916m, 2995w; *ν*(N-H) 3233m, 3262sh.

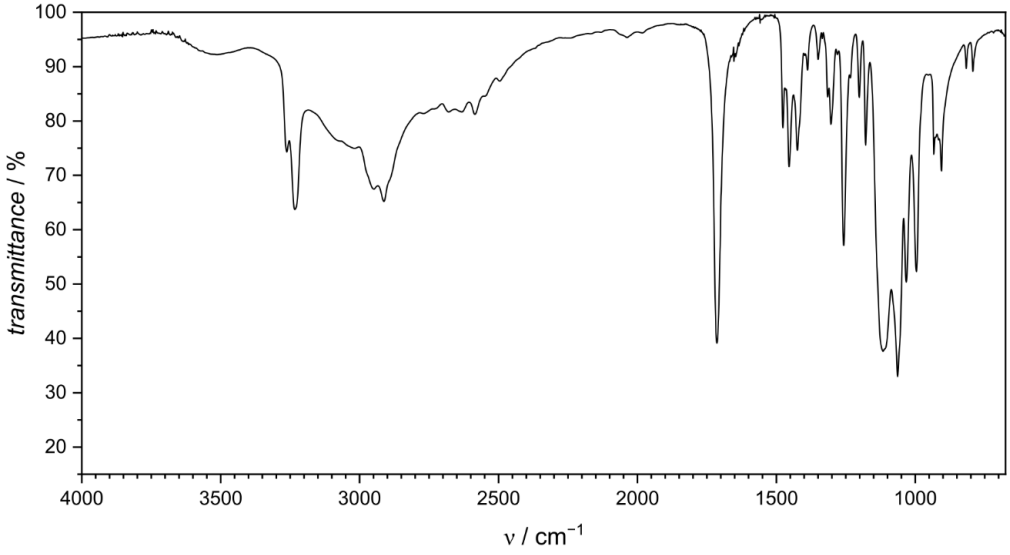

Figure S1. FTIR spectrum of α-[Cu(cyclam(COOH)$_2$)](ClO$_4$)$_2$.

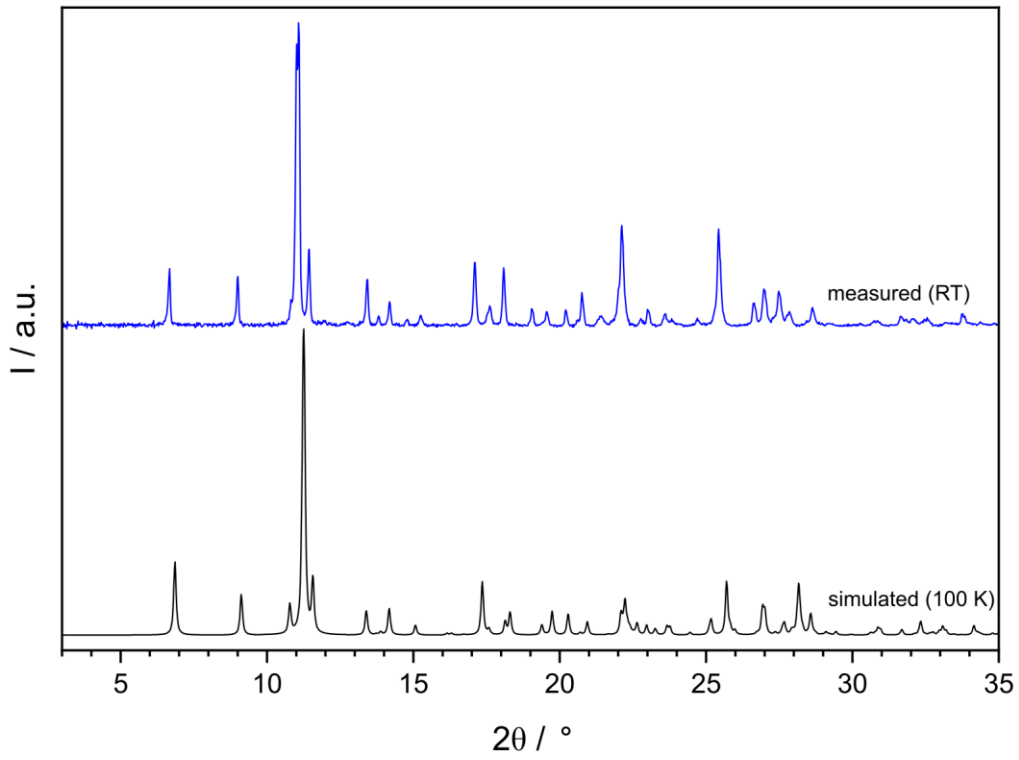

Figure S2. Room temperature powder X-ray diffraction pattern for an as-synthesized sample of α-[Cu(cyclam(COOH)$_2$)](ClO$_4$)$_2$ (blue) compared with the pattern calculated from the single-crystal model[2] (black; 100 K; CCDC refcode: HAWKAR01).

Synthesis of (H$_3$O)$_4${[Cu(cyclam)(COOH)$_2$]$_3$[M(CN)$_8$]$_2$}Cl$_2$ · 10H$_2$O (M = Mo, W)

(H$_3$O)$_4${[Cu^{II}(cyclam)(COOH)$_2$]$_3$[Mo^{IV}(CN)$_8$]$_2$}Cl$_2$ · 10H$_2$O (**1**). Solutions of α-[Cu(cyclam(COOH)$_2$)](ClO$_4$)$_2$ (0.075 mmol, 41.3 mg) in 2.50 mL 1 M HCl and K$_4$[Mo^{IV}(CN)$_8$]·2H$_2$O (0,050 mmol, 24.8 mg) in 1.25 mL of 1 M HCl were prepared and filtered through cotton wool. The solutions were mixed, and the resulting dark orange solution was left in the dark for a week. During this period, purple parallelogram-shaped plate-like crystals of **1** formed. The product was filtered, washed with distilled water, and dried in air. Yield: 77%. EA. Calculated for C$_{52}$H$_{104}$N$_{28}$O$_{26}$Cl$_2$Cu$_3$Mo$_2$: C 31.37, H 5.27, N 19.70 %. Found: C 31.22, H 5.24, N 19.76 %. IR. (cm^{-1}). *ν*(C=O) 1714vs, 1724sh, *ν*(CN) 2115vs, 2122s, 2136sh, 2141vs, 2148sh, 2162w, *ν*(C-H) 2886m, 2945m, *ν*(N-H) 3220m, 3251m, 3264m, *ν*(OH) 3364br, 3485w, 3591w.

(H$_3$O)$_4${[Cu^{II}(cyclam)(COOH)$_2$]$_3$[W^{IV}(CN)$_8$]$_2$}Cl$_2$ · 10H$_2$O (**2**). The compound was obtained analogically to **1** using K$_4$[W^{IV}(CN)$_8$]·2H$_2$O (0.050 mmol, 29.2 mg) instead K$_4$[Mo^{IV}(CN)$_8$]·2H$_2$O. Similarly, compound **2** forms purple, parallelogram-shaped, plate-like crystals. The product was filtered, washed with distilled water, and dried in air. Yield: 73%. EA. Calculated for C$_{52}$H$_{104}$N$_{28}$O$_{26}$Cl$_2$Cu$_3$W$_2$: C 28.82, H 4.84, N 18.10 %. Found: C 28.81, H 4.73, N 18.18 %. IR (cm^{-1}). *ν*(C=O) 1714vs, 1724sh, *ν*(CN) 2113vs, 2121s, 2133vs,

2146sh, 2163w, *v*(C-H) 2885m, 2495m, *v*(N-H) 3220m, 3251m, *v*(O-H) 3263m, 3369br, 3483w, 3591w.

Structure determination. Single-crystal diffraction data were collected at 100 K on a Bruker D8 Quest diffractometer equipped with a Mo Kα radiation source (λ = 0.71073 Å) and a Photon II detector. The crystals of **1** and **2** were covered in a protective layer of NVH oil (Cargille). Unit cell determination, measurement strategy calculation, and data collection were performed with the Bruker APEX3 software. The structures were solved with the intrinsic phasing method using SHELXT[7], and the models were refined against F^2 with SHELXL software.[8] All non-hydrogen atoms were refined as anisotropic. The C-H and N-H hydrogen atoms were placed in the idealized geometry and refined with U_{iso}(H) = 1.2 U_{eq} of the C or N atoms using the riding model. The O-H hydrogen atoms of hydronium cations, water molecules, and carboxylic groups were located at the differential Fourier map, taking into account suitable H-bonds. The O-H distances and H-O-H angles were restrained (DFIX, DANG) and refined with U_{iso}(H) = −1.2 U_{iso}(O). The disordered carbonyl O atom of one of the carboxylic groups was refined in two positions (O24 and O24A) with the PART instruction. Deposition Numbers 2478313 (**1**) and 2478314 (**2**) contain the supplementary crystallographic data for this paper. These data are provided free of charge by the joint Cambridge Crystallographic Data Centre and Fachinformationszentrum Karlsruhe Access Structures service www.ccdc.cam.ac.uk/structures.

Physical measurements. Elemental analysis was performed on an Elementar Vario Cube CHNS analyzer. The infrared spectra were collected on a Thermo Scientific Nicolet iN 10 FTIR microscopic spectrometer in transmission for samples pressed against a polished BaF_2 window. The UV-vis-NIR electronic spectra were collected on a Shimadzu UV-3600i Plus spectrophotometer in diffuse reflectance mode for samples mixed with $BaSO_4$ (~1% w/w). The thermogravimetric analysis was performed in the flow of dry N_2 on a Netzsch TG209 F1 Libra analyzer in the 20-300 °C range with a heating rate of 1 K min^{-1}. The differential scanning calorimetry analysis was performed at a Netzsch DSC214 Polyma analyser in the 223-333 K range at a heating/cooling rate of 10 K min^{-1}. The water sorption isotherms were collected at 295 K on an SMS DVS Resolution apparatus in the range of 0-95% relative humidity with a 2 % step and a dm/dt = 0.002 % min^{-1} mass stability threshold. Powder diffraction patterns were collected for samples packed into glass capillaries on a Bruker D8 Advance ECO diffractometer equipped with CuKα (λ = 1.5406 Å) radiation source. Le Bail analysis of diffraction patterns was performed with expo v2.3.5 software.[9]

Impedance studies. The impedance data were collected with an MTZ-35 electrochemical impedance analyzer equipped with an ITS temperature chamber and a CESH sample holder using the 4-probe method. The powdered samples were pressed into pellets 5 mm in diameter. To provide better electrical contact, the pellets were sputter-coated with gold on both sides using an MCM-100P coater (SEC). The pellets were

placed between gold electrodes in the CESH holder, and their thickness was measured using a digital indicator S_Dial MINI Basic (Sylvac). The data were collected in the 10 MHz–1 Hz frequency range with an input voltage amplitude of 100 mV. Sample conditions were stabilized with an HG-100 (L&C) humidity generator. The dependence of conductivity on relative humidity (RH) was measured at 298 K in the 20-95% RH range (accuracy of ± 2% RH) for pellets 0.615 mm (**1**) and 0.337 mm (**2**) thick. At each RH step, impedance data were collected every 10 minutes until there was a minimal change in the spectrum in at least three subsequent cycles. The temperature dependence of conductivity was measured for the pellets, 0.319 mm (**1**) and 0.217 mm (**2**) thick, in the range of 255–323 K, with a temperature stabilization time of 20 min at each step. Prior to the measurement, the samples were stabilized at 50% RH at 298 K. The resistance of the samples was determined by fitting an equivalent circuit model using EC-Lab v11.52 software by BioLogic. The used equivalent circuit model, $(Q_b/R_b)+(Q_g/R_g)+Q_{el}$, includes resistance (R) and capacitance (Q, constant phase element) of bulk (b) and grain boundary (g), as well as the capacitance of the electrode polarization (Q_{el}). The total resistance of the materials was obtained as the sum of bulk and grain boundary resistance ($R_t = R_b+R_g$). The conductivity (σ) was calculated as $\sigma = d/(A \cdot R_t)$ [S cm^{-1}], where d and A are the pellet thickness and the contact area, respectively.

Magnetic and photoirradiation studies. Magnetic and photomagnetic studies were performed on a Quantum Design MPMS3 SQUID magnetometer. Direct current magnetic susceptibility was investigated in the 300–2 K range at 1 kOe applied field and isothermal magnetization at 2 K in the magnetic field up to 70 kOe. The diamagnetic contributions coming from the samples and holders were subtracted from the data. Photomagnetic measurements were performed on samples placed in a thin layer between two layers of Scotch tape and mounted in a plastic straw. The sample was inserted into the magnetometer at 250 K, and then, the sample chamber was pumped to avoid sample dehydration. The photoirradiation was performed using a 450 nm laser diode with a light power of 10 mW cm^{-2} (measured at the sample). The sample mass and diamagnetic corrections were determined by comparison to bulk measurements. The FTIR photoirradiation experiments were performed on samples placed in a Linkam THMS350V optical cryostat and irradiated, evacuated at 250 K with the 450 nm laser diode at 90 K for 60-90 min. The spectra were taken before and after irradiation, as well as after thermal relaxation.

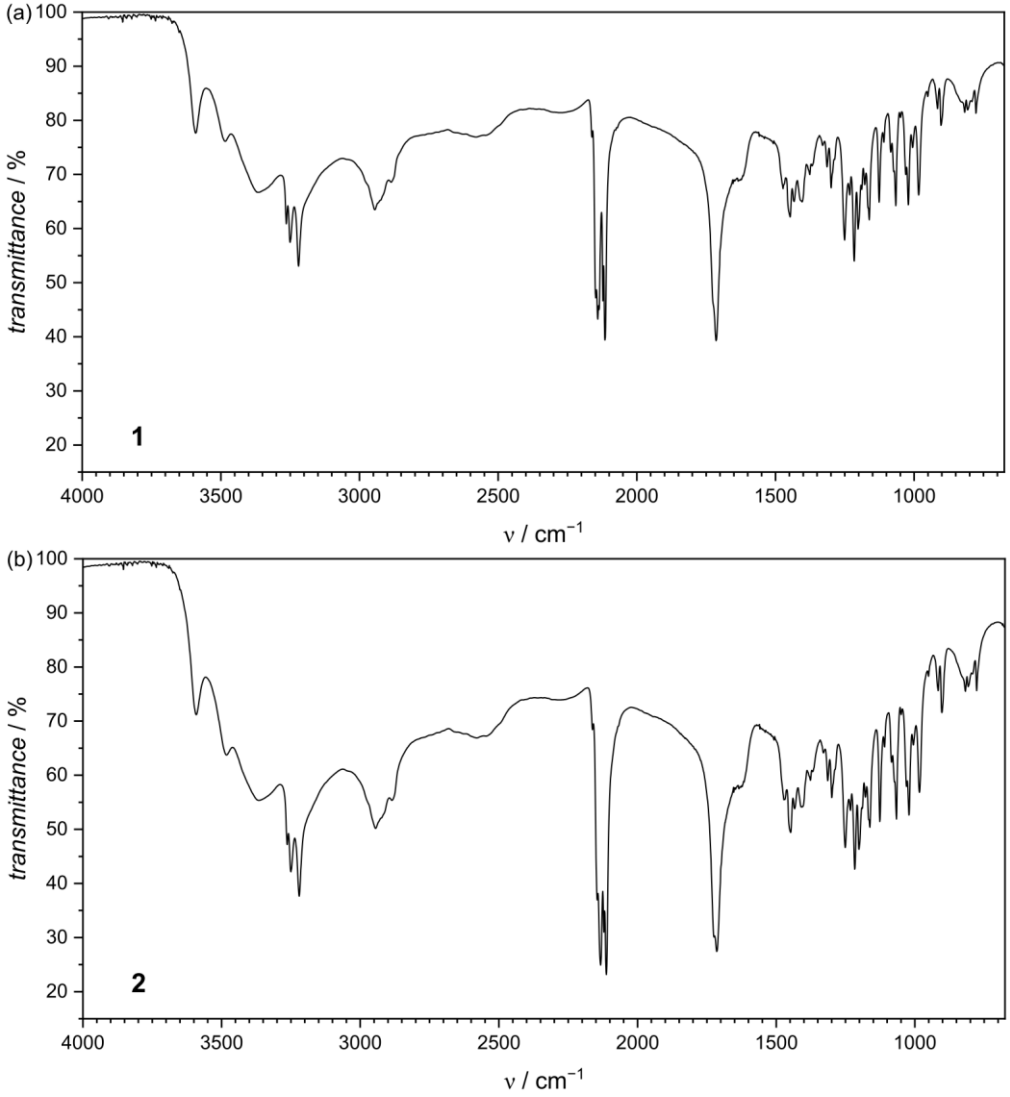

Figure S3. FTIR spectra of **1** (a) and **2** (b).

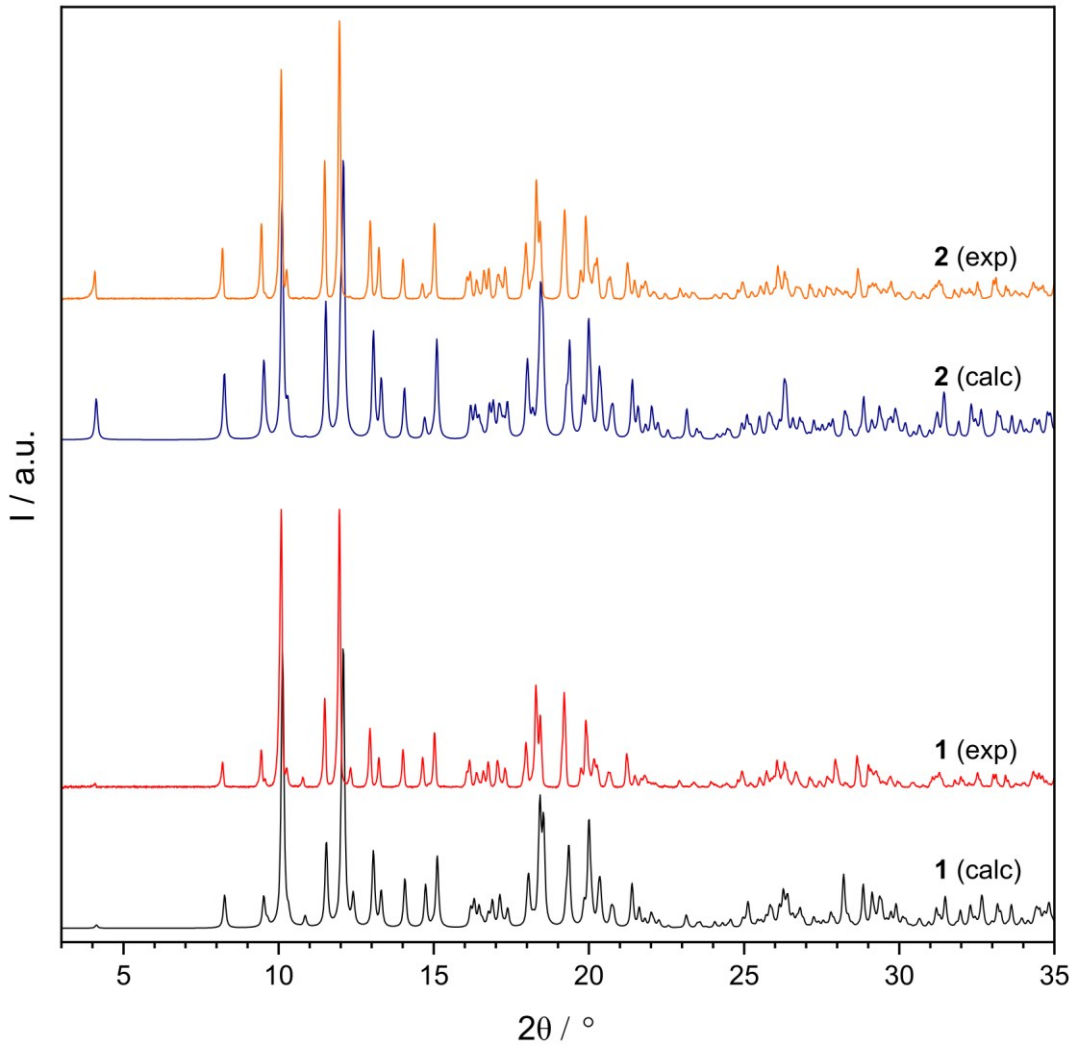

Figure S4. A comparison of powder XRD patterns measured at room temperature (exp) and calculated from the single-crystal model (100 K; calc) for **1** and **2**.

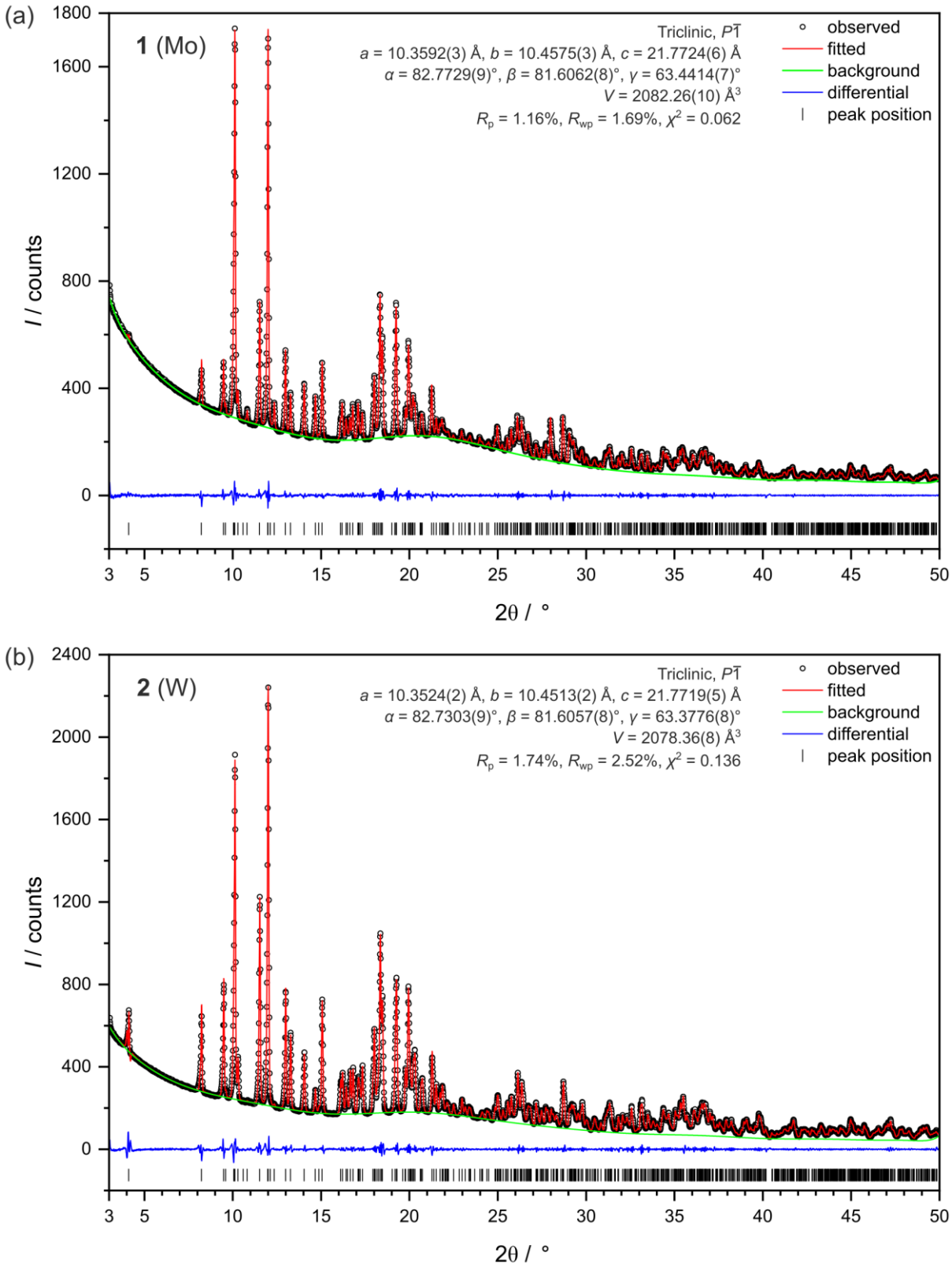

Figure S5. Le Bail profile fitting for diffraction patterns of **1** (a) and **2** (b) collected at room temperature.

Table S1. Selected crystal data and details of structure refinement for **1** and **2**.

	1	**2**
		crystal data
formula	$C_{52}H_{104}Cl_2Cu_3Mo_2N_{28}O_{26}$	$C_{52}H_{104}Cl_2Cu_3N_{28}O_{26}W_2$
M_r **/ g·mol^{-1}**	1991.03	2166.85
radiation type	Mo *Kα* radiation, λ = 0.71073	
crystal system	triclinic	triclinic
space group	$P\bar{1}$	$P\bar{1}$
***T* / K**	100(2)	100(2)
***a* / Å**	10.3184(6)	10.3232(6)
***b* / Å**	10.4261 (6)	10.4395(6)
***c* / Å**	21.6647(13)	21.6921(13)
α / °	82.711(2)	82.633(2)
β / °	81.791(2)	81.751(2)
γ / °	63.177(2)	62.973(2)
***V* / Å^3**	2053.5(2)	2055.6(2)
Z	1	1
calculated density / g·cm^{-3}	1.610	1.750
μ / mm^{-1}	1.22	3.71
***F*(000)**	1025	1089
crystal size / mm × mm × mm	0.43 × 0.32 × 0.07	0.16 × 0.15 × 0.09
		data collection
***θ* range**	2.2°–29.3°	2.5°–27.9°
limiting indices	h = –14→14 k = –14→14 l = –29→28	h = –13→13 k = –13→13 l = –28→28
measured reflections	63458	40462
independent reflections	11162	9791
observed reflections $I > 2\sigma(I)$	10410	9413
R_{int}	0.027	0.024
completeness / %	99.8	99.8
		refinement
refinement method	full-matrix least-squares on F^2	
data / parameters / restraints	11162 / 578 / 30	9791 / 578 / 30
GoF on F^2	1.09	1.07
final *R* indices	$R[F^2 > 2\sigma(F^2)]$ = 0.026 $wR(F^2)$ = 0.057 $w = 1/[\sigma^2(F_o^2) + (0.0179P)^2 + 1.9465P]$	$R[F^2 > 2\sigma(F^2)]$ = 0.019 $wR(F^2)$ = 0.043 $w = 1/[\sigma^2(F_o^2) + (0.0132P)^2 + 2.7779P]$
	$P = (F_o^2 + 2F_c^2)/3$	
largest diff. peak/hole / e·Å^{-3}	0.45 / –0.49	0.88 / −0.63
CCDC deposition number	2478313	2478314

Table S2. Selected bond lengths (Å) and angles (°) in the structure of **1** and **2** at 100 K.

	1 (M = Mo)	**2** (M = W)
M1—C1	2.1737(16)	2.175(2)
M1—C2	2.1528(15)	2.160(2)
M1—C3	2.1590(16)	2.163(2)
M1—C4	2.1531(16)	2.157(2)
M1—C5	2.1501(16)	2.154(2)
M1—C6	2.1583(16)	2.163(2)
M1—C7	2.1480(16)	2.154(2)
M1—C8	2.1652(16)	2.168(2)
Cu1—N1	2.5261(14)	2.5228(19)
Cu1—N11	2.0294(13)	2.0297(18)
Cu1—N12	2.0198(13)	2.0189(17)
Cu2—N2	2.2375(13)	2.2401(18)
Cu2—N21	2.0199(13)	2.0195(18)
Cu2—N22	2.0211(13)	2.0245(18)
Cu2—N23	2.0349(13)	2.0329(18)
Cu2—N24	2.0378(13)	2.0404(18)
C16—O11 (H)	1.319(2)	1.316(3)
C16—O12	1.210(2)	1.211(3)
C31—O21 (H)	1.322(2)	1.321(3)
C31—O22	1.216(2)	1.216(3)
C32—O23 (H)	1.291(2)	1.293(3)
C32—O24	1.207(4)	1.189(7)
C32—O24*A*	1.251(4)	1.256(7)
M1—C1—N1	177.60(14)	177.81(19)
M1—C2—N2	176.69(13)	176.79(18)
C1—M1—C2	142.20(6)	142.08(8)
C1—N1—Cu1	153.31(13)	153.56(17)
C2—N2—Cu2	167.62(13)	167.59(17)
N11—Cu1—N12	94.23(5)	94.23(7)
N11—Cu1—N12^{i}	85.77(5)	85.77(7)
N11—Cu1—N1	93.04(5)	93.25(7)
N11^{i}—Cu1—N1	86.96(5)	86.75(7)
N12—Cu1—N1	90.71(5)	90.71(7)
N12^{i}—Cu1—N1	89.29(5)	89.29(7)
N21—Cu2—N22	85.92(5)	86.09(7)
N22—Cu2—N23	93.25(5)	93.22(7)
N23—Cu2—N24	85.29(5)	85.17(7)
N21—Cu2—N24	94.48(5)	94.48(7)
N21—Cu2—N2	94.61(5)	94.36(7)
N22—Cu2—N2	96.44(5)	96.27(7)
N23—Cu2—N2	92.00(5)	92.09(7)
N24—Cu2—N2	92.83(5)	92.95(7)
Symmetry code: (i) −*x*+2, −*y*, −*z*+1		

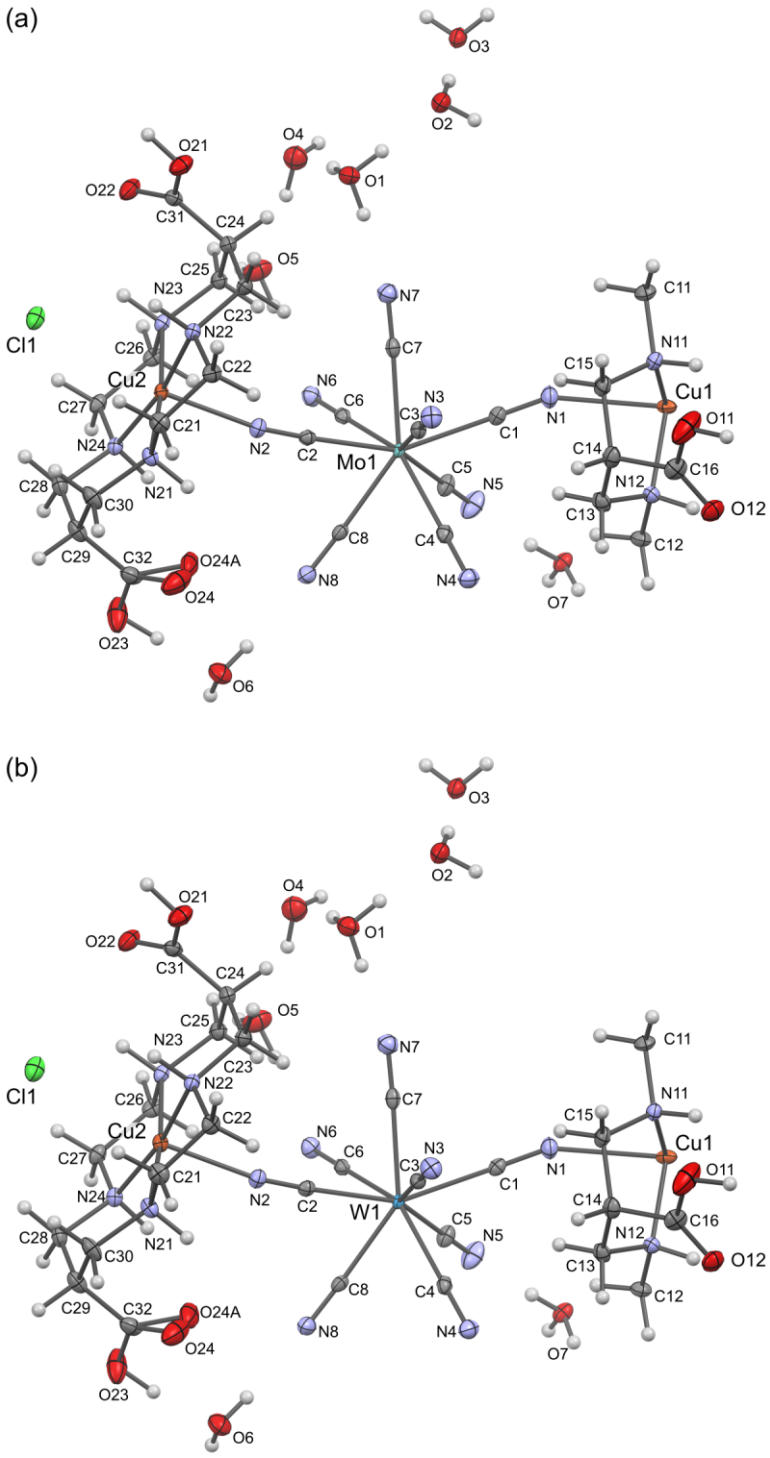

Figure S6. Asymmetric units of **1** (a) and **2** (b). The thermal displacement ellipsoids are drawn for 50% probability.

Table S3. Continuous Shape Measures parameters (CShM[a]) for metallic centers in the structures of **1** and **2**.

	1 (M1 = Mo)			**2** (M1 = W)		
Cu1	OC-6[b]			OC-6		
	1.285			1.281		
Cu2	vOC-5		SPY-5	vOC-5		SPY-5
	0.557		0.731	0.552		0.733
M1	SAPR-8	BTPR-8	TDD-8	SAPR-8	BTPR-8	TDD-8
	0.279	1.764	2.027	0.266	1.772	2.084

a) CShM = 0 corresponds to an ideal geometry; b) OC-6 – octahedron (O_h), vOC-5 – vacant octahedron (C_{4v}), SPY-5 – spherical square pyramid (C_{4v}), SAPR-8 – square antiprism (D_{4d}), BTPR-8 – biaugmented trigonal prism (C_{2v}), TDD-8 – triangular dodecahedron (D_{2d}).

Table S4. The Cu^{II}-Cl bond lengths in selected *trans*-[Cu(macrocycle)]$^{2+}$ complexes with cyclam-like macrocycles.

CCDC Refcode[10]	**Cu–Cl / Å**	**T / K**	**Reference**
DAPXOI	2.700	100	[11]
EVABEI	2.844	100	[12]
FODWAZ	2.798	120	[13]
	2.812	120	
ISIZUI	2.834	95	[14]
ISOBAW	2.945	120	[14]
JEZDEB	2.543	120	[15]
	2.550	120	
KEQYEM	2.832	110	[16]
	2.840	110	
	2.793	110	
	2.844	110	
QASKUU	2.804	100	[17]
	2.814	100	
	2.811	100	
	2.817	100	
QONCUS	2.721	100	[18]
TALSOQ	2.731	100	[19]
VERSOD	2.868	100	[20]
YESQOF	2.836	100	[2]
YOFCAB	2.785	100	[21]
average	2.787		
median	2.812		
1	3.109	100	this work
2	3.105	100	this work

Table S5. Hydrogen-bond geometry in **1** and **2** at 100 K.

D—H···A	**D—H** / Å	**H···A** / Å	**D···A** / Å	**D—H···A** / °
				1 (M = Mo)
N12—H12···O12	1.00	2.19	2.8845(18)	126
N21—H21···O12^{ii}	1.00	2.10	2.9997(18)	148
N21—H21···O24	1.00	2.20	2.848(5)	121
N22—H22···O3^{iii}	1.00	2.18	3.0543(18)	144
N22—H22···Cl1	1.00	2.74	3.3845(13)	123
N23—H23···O22	1.00	2.30	2.9726(18)	123
N23—H23···Cl1	1.00	2.71	3.3591(13)	123
N24—H24*A*···O2^{iv}	1.00	2.17	3.0274(18)	143
O1—H1*A*···O2	0.87(2)	1.65(2)	2.5264(18)	177(2)
O1—H1*B*···N7	0.86(2)	1.73(2)	2.5877(19)	176(2)
O1—H1*C*···O4	0.89(2)	1.57(2)	2.4553(19)	172(2)
O2—H2*A*···N8^{v}	0.82(2)	2.07(2)	2.8808(19)	177(2)
O2—H2*B*···O3	0.84(2)	1.82(2)	2.6581(19)	174(2)
O3—H3*A*···O22^{vi}	0.81(2)	2.02(2)	2.8190(17)	169(2)
O3—H3*B*···N6^{v}	0.81(2)	2.06(2)	2.8216(18)	159(2)
O4—H4*A*···Cl1^{vii}	0.86(2)	2.19(2)	3.0582(15)	178(2)
O4—H4*B*···O5	0.87(2)	1.77(2)	2.639(2)	172(2)
O5—H5*A*···N6	0.82(2)	2.06(2)	2.872(2)	175(2)
O5—H5*B*···Cl1^{viii}	0.84(2)	2.27(2)	3.0939(15)	170(2)
O6—H6*A*···N8	0.83(2)	2.05(2)	2.877(2)	175(2)
O6—H6*B*···N7^{iv}	0.84(2)	2.30(2)	3.016(2)	143(2)
O7—H7*A*···N3^{ix}	0.84(1)	1.77(2)	2.6115(18)	177(2)
O7—H7*B*···N4^{x}	0.85(1)	1.75(2)	2.6009(19)	178(2)
O7—H7*C*···N5	0.86(1)	1.70(2)	2.5471(19)	174(2)
O11—H11*O*···O24^{ii}	0.94(2)	1.82(2)	2.692(9)	153(3)
O11—H11*O*···O24*A*^{ii}	0.94(2)	1.70(2)	2.630(6)	169(3)
O21—H21*O*···Cl1^{xi}	0.94(2)	2.11(2)	3.0129(13)	163(2)
O23—H23*O*···O6	0.98(2)	1.61(2)	2.589(2)	172(2)
				2 (M = W)
N12—H12···O12	1.00	2.19	2.883(2)	125
N21—H21···O12^{ii}	1.00	2.11	3.007(2)	148
N21—H21···O24	1.00	2.19	2.837(7)	121
N22—H22···O3^{iii}	1.00	2.18	3.051(2)	144
N22—H22···Cl1	1.00	2.74	3.3825(18)	123
N23—H23···O22	1.00	2.30	2.969(2)	123
N23—H23···Cl1	1.00	2.70	3.3546(19)	123
N24—H24*A*···O2^{iv}	1.00	2.16	3.020(2)	143
O1—H1*A*···O2	0.87(2)	1.67(2)	2.538(2)	177(3)
O1—H1*B*···N7	0.86(2)	1.74 (2)	2.600(3)	177(3)
O1—H1*C*···O4	0.87(2)	1.60(2)	2.458(3)	169(3)
O2—H2*A*···N8^{v}	0.86(2)	2.04(2)	2.891(3)	177(3)
O2—H2*B*···O3	0.85(2)	1.81(2)	2.660(2)	175(3)
O3—H3*A*···O22^{vi}	0.83(2)	2.01(2)	2.822(2)	170(3)
O3—H3*B*···N6^{v}	0.82(2)	2.06(2)	2.827(3)	155(3)
O4—H4*A*···Cl1^{vii}	0.88(2)	2.17(2)	3.050(2)	172(3)
O4—H4*B*···O5	0.88(2)	1.77(2)	2.636(3)	168(3)
O5—H5*A*···N6	0.83(2)	2.06(2)	2.882(3)	171(3)
O5—H5*B*···Cl1^{viii}	0.85(2)	2.25(2)	3.087(2)	172(3)
O6—H6*A*···N8	0.85(2)	2.03(2)	2.873(3)	175(3)

Symmetry codes: (ii) −*x*+1, −*y*+1, −*z*+1; (iii) *x*−1, *y*+1, *z*; (iv) *x*, *y*+1, *z*; (v) *x*, *y*−1, *z*; (vi) −*x*+1, −*y*, −*z*+2; (vii) *x*+1, *y*−1, *z*; (viii) −*x*+1, −*y*+1, −*z*+2; (ix) *x*+1, *y*, *z*; (x) −*x*+2, −*y*+1, −*z*+1; (xi) −*x*, −*y*+1, −*z*+2.

Table S5. continued

D—H···A	**D—H** / Å	**H···A** / Å	**D···A** / Å	**D—H···A** / °
				2 (M = W)
O6—H6*B*···N7^{iv}	0.82(2)	2.32(2)	3.009(3)	142(3)
O7—H7*A*···N3^{ix}	0.86(2)	1.76(2)	2.618(2)	179(3)
O7—H7*B*···N4^{x}	0.85(2)	1.77(2)	2.604(2)	170(3)
O7—H7*C*···N5	0.85(2)	1.70(2)	2.545(3)	176(3)
O11—H11*O*···O24^{ii}	0.95(2)	1.78(3)	2.712(17)	166(3)
O11—H11*O*···O24*A*^{ii}	0.95(2)	1.70(2)	2.627(8)	164(3)
O21—H21*O*···Cl1^{xi}	0.96(2)	2.08(2)	3.0143(18)	164(3)
O23—H23*O*···O6	0.96(2)	1.64(2)	2.590(3)	171(3)

Symmetry codes: (ii) −*x*+1, −*y*+1, −*z*+1; (iii) *x*−1, *y*+1, *z*; (iv) *x*, *y*+1, *z*; (v) *x*, *y*−1, *z*; (vi) −*x*+1, −*y*, −*z*+2; (vii) *x*+1, *y*−1, *z*; (viii) −*x*+1, −*y*+1, −*z*+2; (ix) *x*+1, *y*, *z*; (x) −*x*+2, −*y*+1, −*z*+1; (xi) −*x*, −*y*+1, −*z*+2.

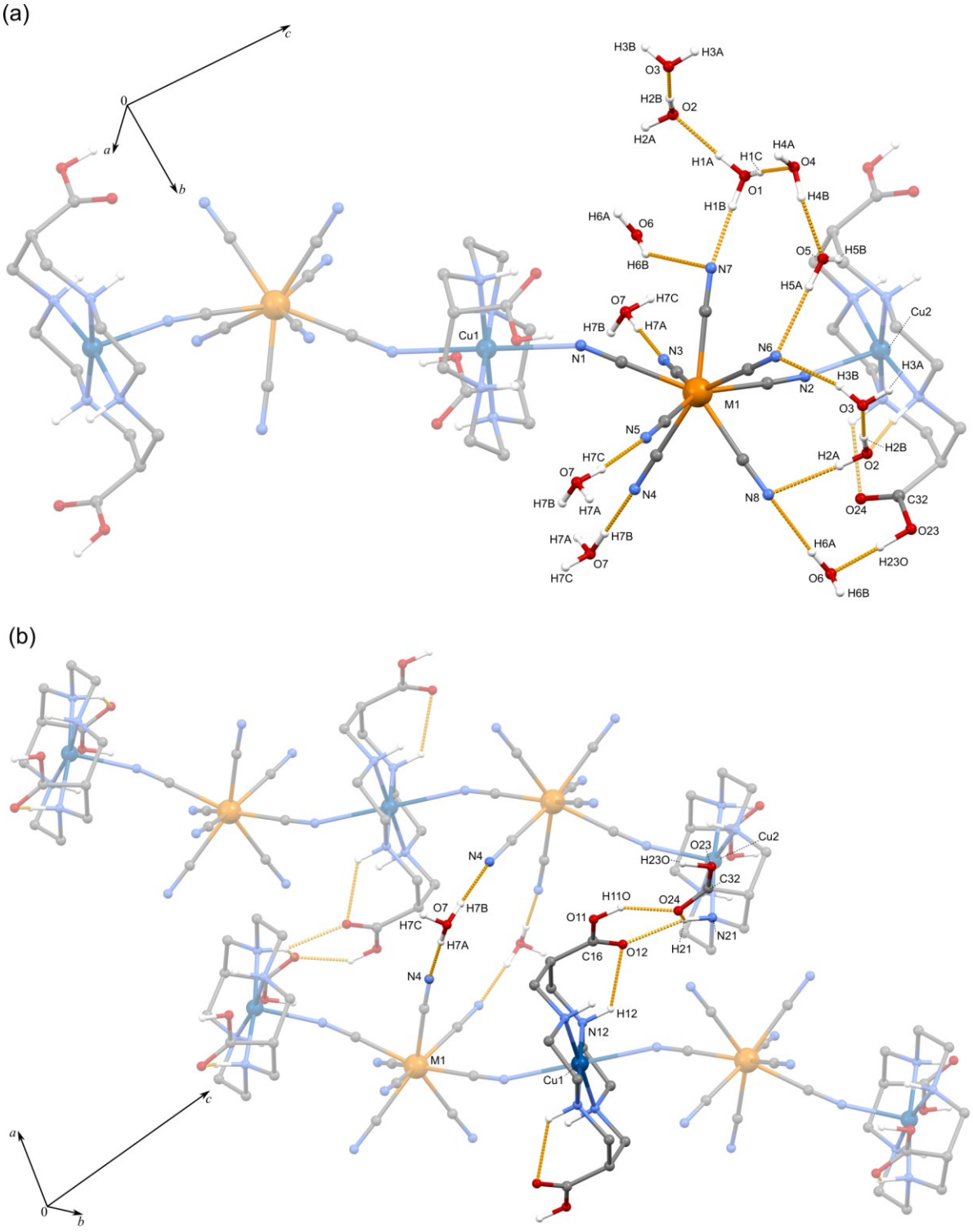

Figure S7. Fragments of the crystal structure showing selected hydrogen bonds formed by octacyanidometallate(IV) anions (a) and the central $[Cu(cyclam(COOH)_2)]^{2+}$ complex (b). The latter forms direct H-bonds with adjacent $\{Cu_3M_2\}^{2-}$ molecules, which result in a motif of supramolecular ribbons. Some H atoms were omitted for clarity.

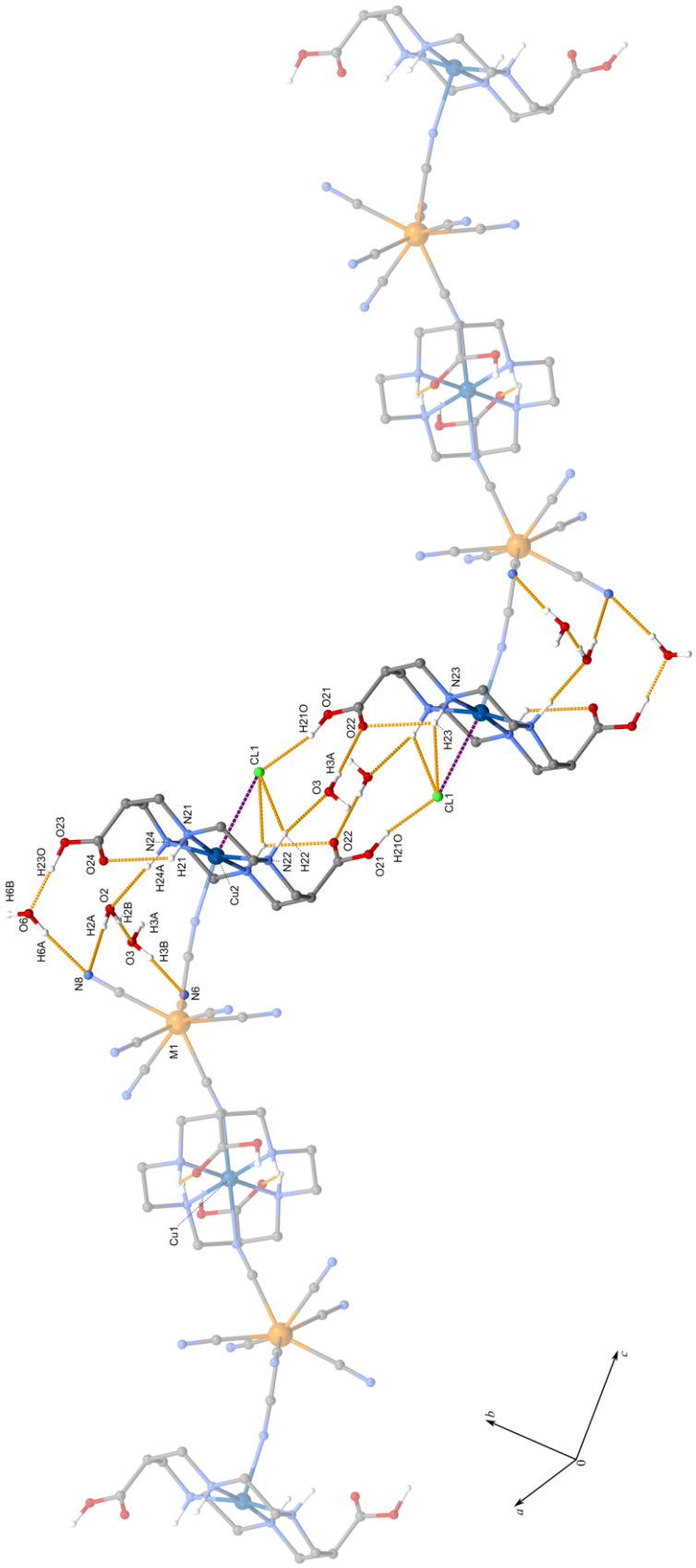

Figure S8. The hydrogen bonds (orange contacts) formed by the terminal $[Cu(cyclam(COOH)_2]^{2+}$ complexes. The purple contacts present the semicoordination Cu-Cl interactions. Some H atoms were omitted for clarity.

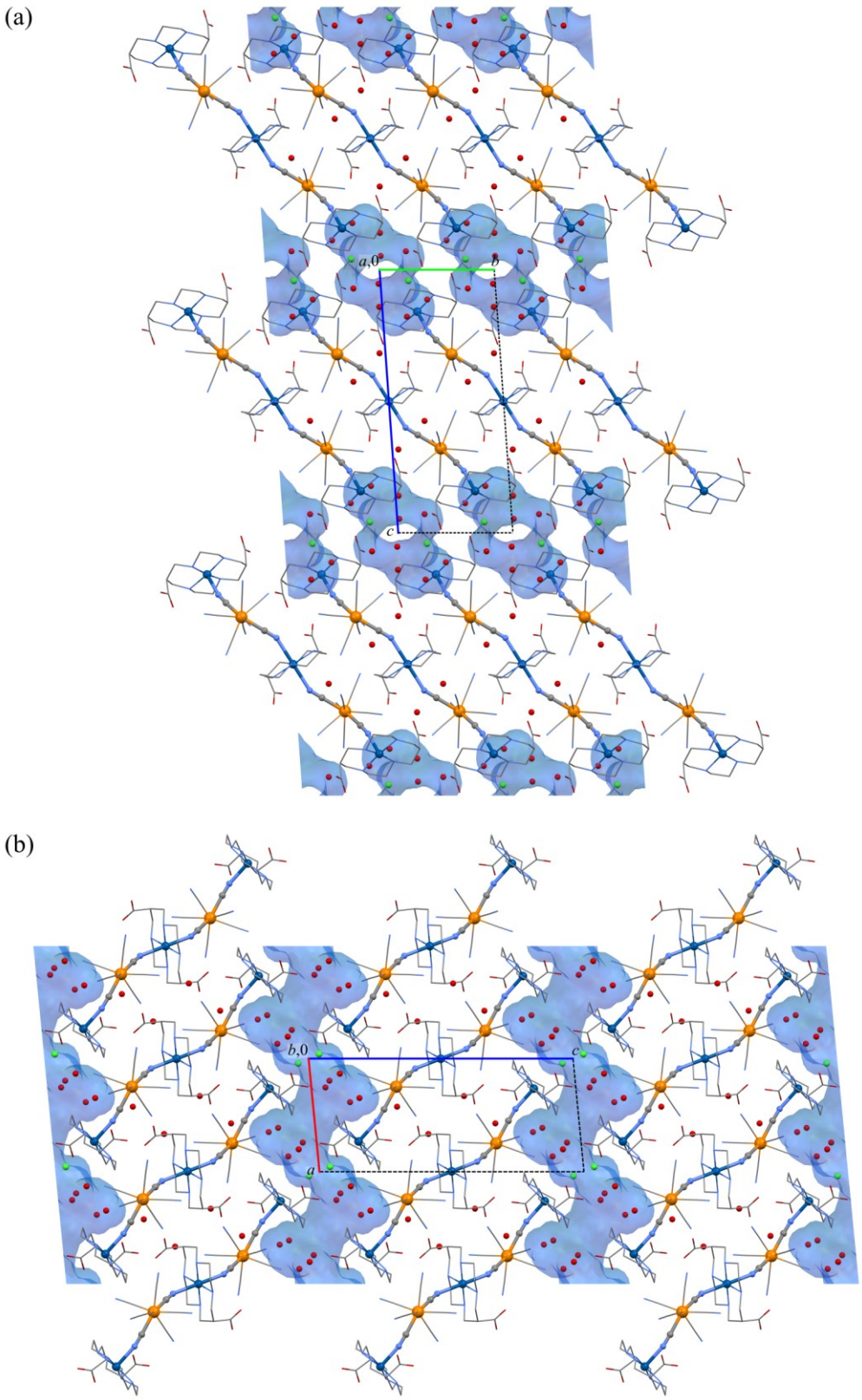

Figure S9. Packing diagrams for **1** with channels filled with H_2O molecules, Cl^-, and H_3O^+ ions (calculated as solvent accessible volume using Mercury 4.0 with probe radius of 1.3 Å and grid spacing of 0.5 Å). H atoms were omitted for clarity.

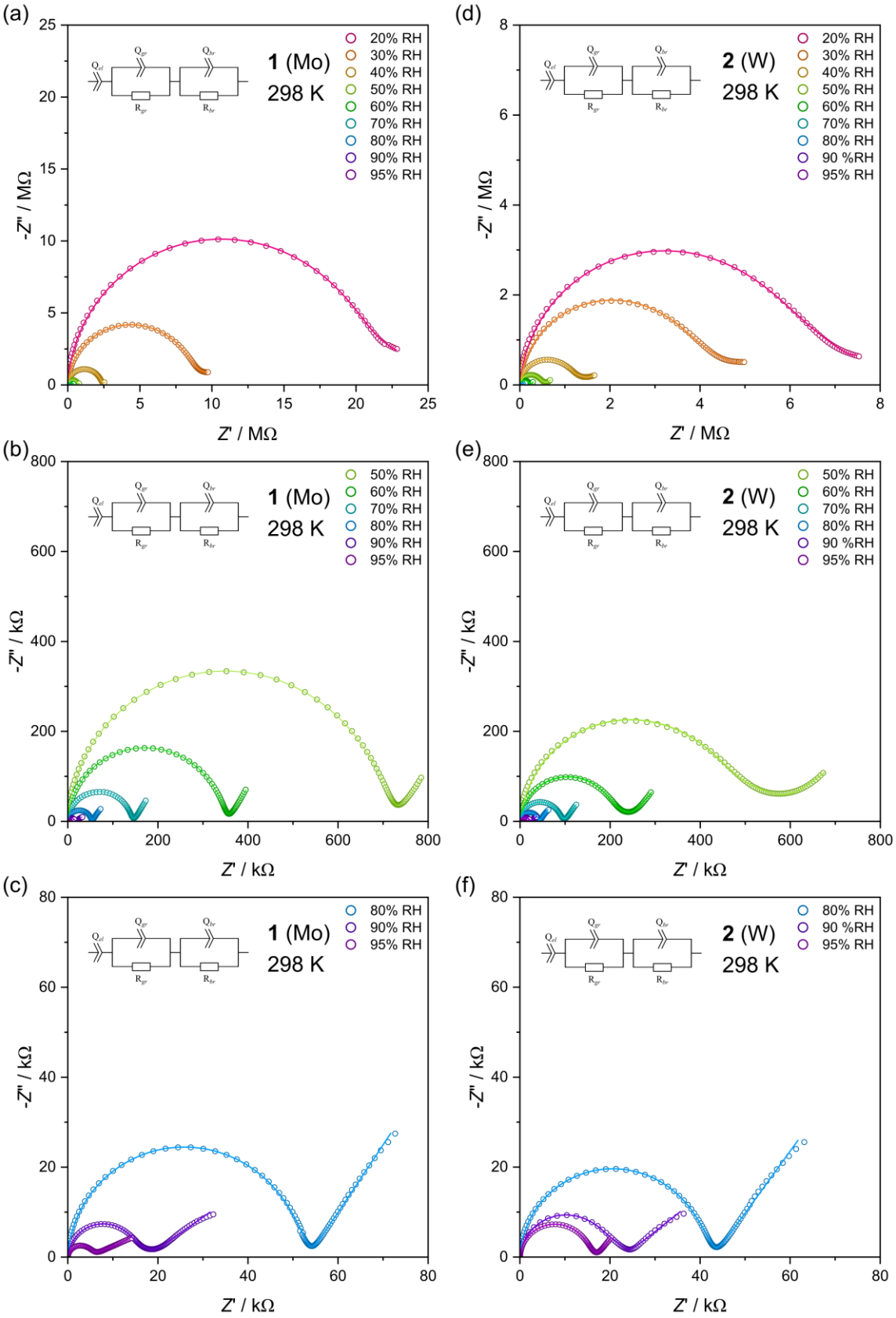

Figure S10. Nyquist plots for 1 (a-c) and 2 (d-f) collected at various relative humidities at 298 K. The solid lines represent fits for the given equivalent circuits.

Table S6. Dependence of conductivity on relative humidity (RH) in **1** and **2** at 298 K.

	σ / S cm^{-1}	
RH / %	**1**	**2**
20	$1.33(1)\cdot10^{-8}$	$1.91(2)\cdot10^{-8}$
30	$3.27(3)\cdot10^{-8}$	$3.64(4)\cdot10^{-8}$
40	$1.30(1)\cdot10^{-7}$	$1.17(1)\cdot10^{-7}$
50	$4.32(5)\cdot10^{-7}$	$3.03(3)\cdot10^{-7}$
60	$8.82(8)\cdot10^{-7}$	$7.08(6)\cdot10^{-7}$
70	$2.15(1)\cdot10^{-6}$	$1.75(2)\cdot10^{-6}$
80	$5.82(6)\cdot10^{-6}$	$3.94(7)\cdot10^{-6}$
90	$1.77(2)\cdot10^{-5}$	$7.27(19)\cdot10^{-6}$
95	$3.88(7)\cdot10^{-5}$	$1.02(1)\cdot10^{-5}$

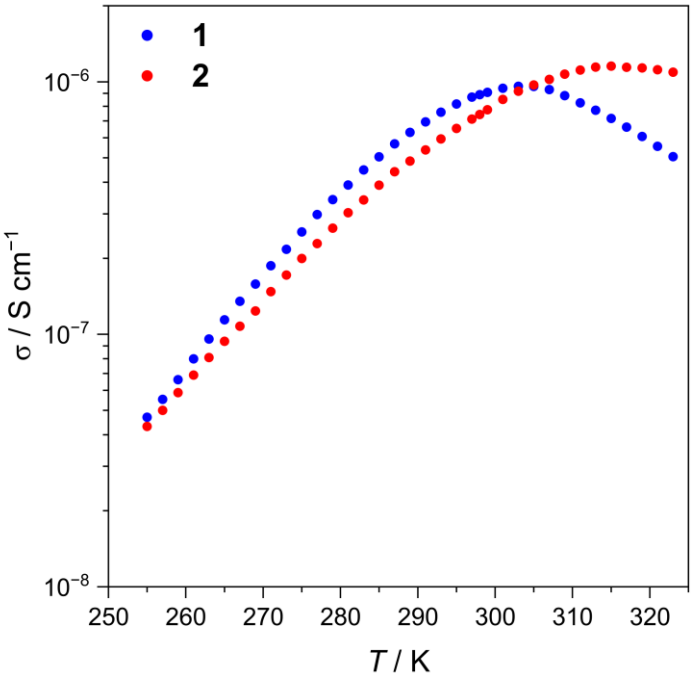

Figure S11. Temperature dependence of conductivity in **1** and **2** at 50% RH.

Table S7. Temperature dependence of conductivity in **1** and **2** at 50% RH.

	σ / S cm^{-1}	
T / K	**1**	**2**
255	$4.69(4)\cdot10^{-8}$	$4.32(4)\cdot10^{-8}$
257	$5.53(5)\cdot10^{-8}$	$5.00(5)\cdot10^{-8}$
259	$6.61(6)\cdot10^{-8}$	$5.87(5)\cdot10^{-8}$
261	$7.99(7)\cdot10^{-8}$	$6.89(6)\cdot10^{-8}$
263	$9.58(8)\cdot10^{-8}$	$8.09(7)\cdot10^{-8}$
265	$1.14(1)\cdot10^{-7}$	$9.39(9)\cdot10^{-8}$
267	$1.35(1)\cdot10^{-7}$	$1.08(1)\cdot10^{-7}$
269	$1.58(1)\cdot10^{-7}$	$1.24(1)\cdot10^{-7}$
271	$1.87(2)\cdot10^{-7}$	$1.48(1)\cdot10^{-7}$
273	$2.17(2)\cdot10^{-7}$	$1.72(2)\cdot10^{-7}$
275	$2.54(2)\cdot10^{-7}$	$2.00(2)\cdot10^{-7}$
277	$2.98(3)\cdot10^{-7}$	$2.29(2)\cdot10^{-7}$
279	$3.42(3)\cdot10^{-7}$	$2.63(2)\cdot10^{-7}$
281	$3.90(3)\cdot10^{-7}$	$3.03(3)\cdot10^{-7}$
283	$4.48(4)\cdot10^{-7}$	$3.40(3)\cdot10^{-7}$
285	$5.05(4)\cdot10^{-7}$	$3.90(4)\cdot10^{-7}$
287	$5.68(5)\cdot10^{-7}$	$4.40(4)\cdot10^{-7}$
289	$6.31(5)\cdot10^{-7}$	$4.85(4)\cdot10^{-7}$
291	$6.94(6)\cdot10^{-7}$	$5.36(5)\cdot10^{-7}$
293	$7.58(7)\cdot10^{-7}$	$5.94(5)\cdot10^{-7}$
295	$8.17(7)\cdot10^{-7}$	$6.53(6)\cdot10^{-7}$
297	$8.69(7)\cdot10^{-7}$	$7.12(7)\cdot10^{-7}$
298	$8.90(8)\cdot10^{-7}$	$7.42(7)\cdot10^{-7}$
299	$9.08(8)\cdot10^{-7}$	$7.75(7)\cdot10^{-7}$
301	$9.42(8)\cdot10^{-7}$	$8.51(8)\cdot10^{-7}$
303	$9.60(8)\cdot10^{-7}$	$9.18(8)\cdot10^{-7}$
305	$9.58(8)\cdot10^{-7}$	$9.72(9)\cdot10^{-7}$
307	$9.32(8)\cdot10^{-7}$	$1.02(9)\cdot10^{-6}$
309	$8.82(8)\cdot10^{-7}$	$1.07(1)\cdot10^{-6}$
311	$8.25(7)\cdot10^{-7}$	$1.11(1)\cdot10^{-6}$
313	$7.71(7)\cdot10^{-7}$	$1.14(1)\cdot10^{-6}$
315	$7.16(6)\cdot10^{-7}$	$1.15(1)\cdot10^{-6}$
317	$6.61(6)\cdot10^{-7}$	$1.14(1)\cdot10^{-6}$
319	$6.08(5)\cdot10^{-7}$	$1.14(1)\cdot10^{-6}$
321	$5.55(5)\cdot10^{-7}$	$1.12(1)\cdot10^{-6}$
323	$5.05(4)\cdot10^{-7}$	$1.09(1)\cdot10^{-6}$

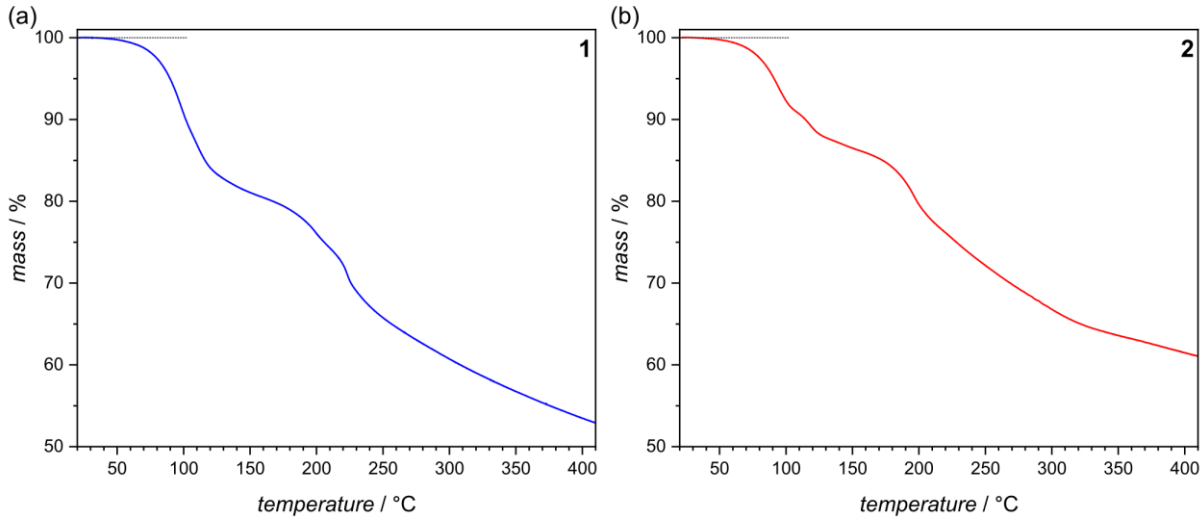

Figure S12. Thermogravimetric analysis for **1** (a) and **2** (b) performed with a heating rate of 1 K min^{-1} in dry nitrogen flow.

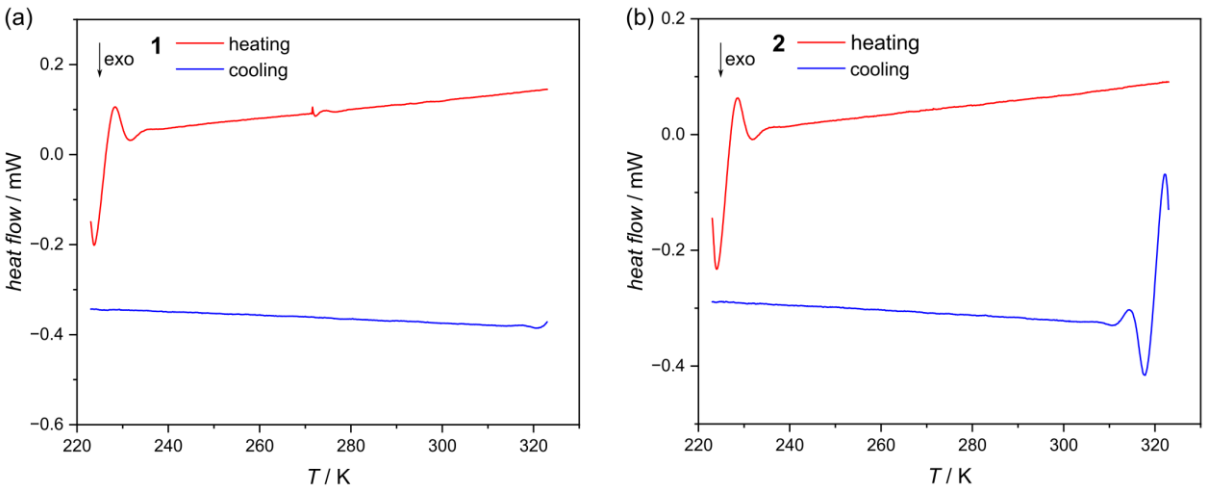

Figure S13. Differential scanning calorimetry profiles of **1** (a) and **2** (b) recorded at a heating/cooling rate of 10 K min^{-1}.

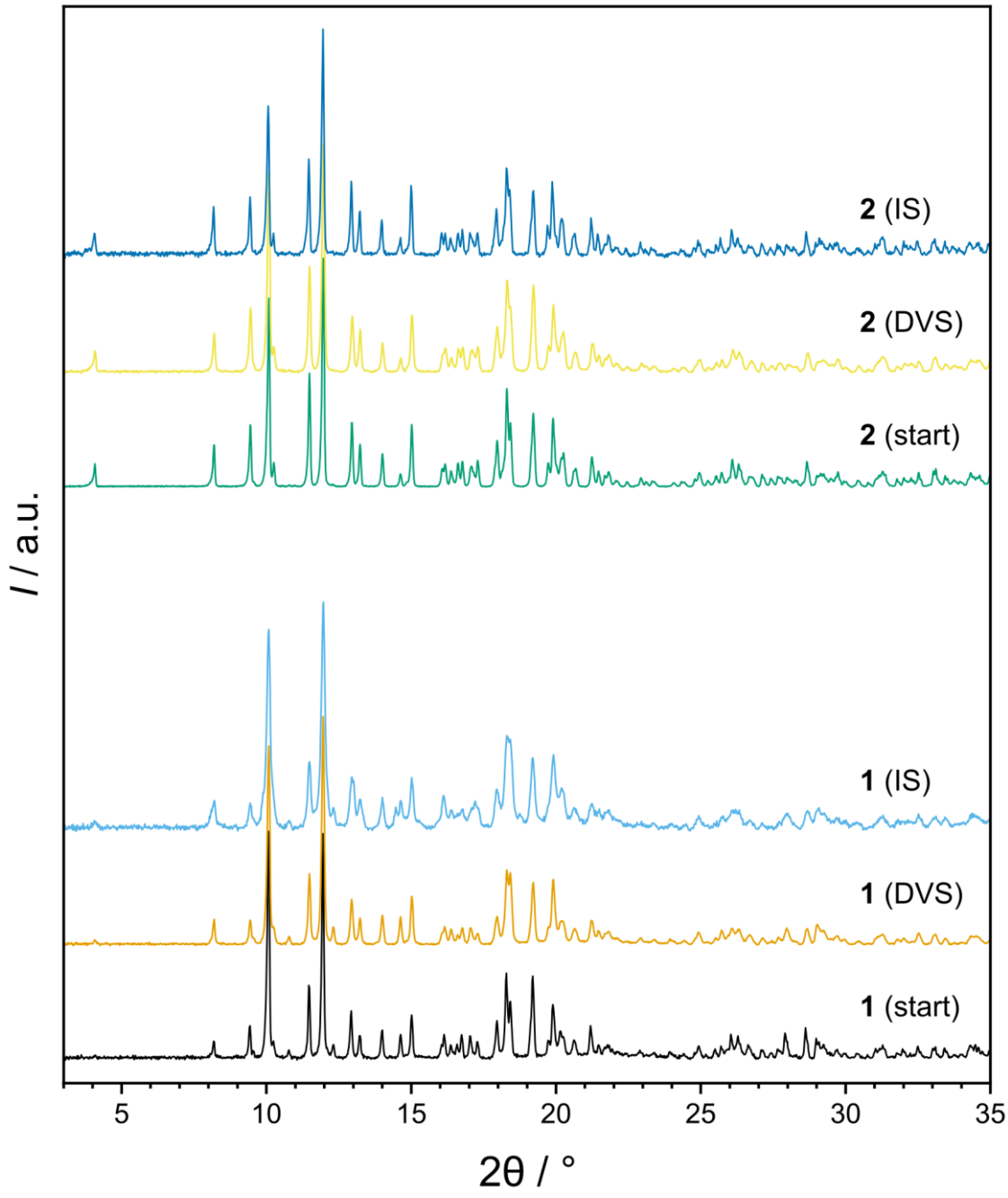

Figure S14. PXRD patterns recorded for **1** and **2** before (start) and after the dynamic vapor sorption (DVS) and impedance spectroscopy (IS) experiments.

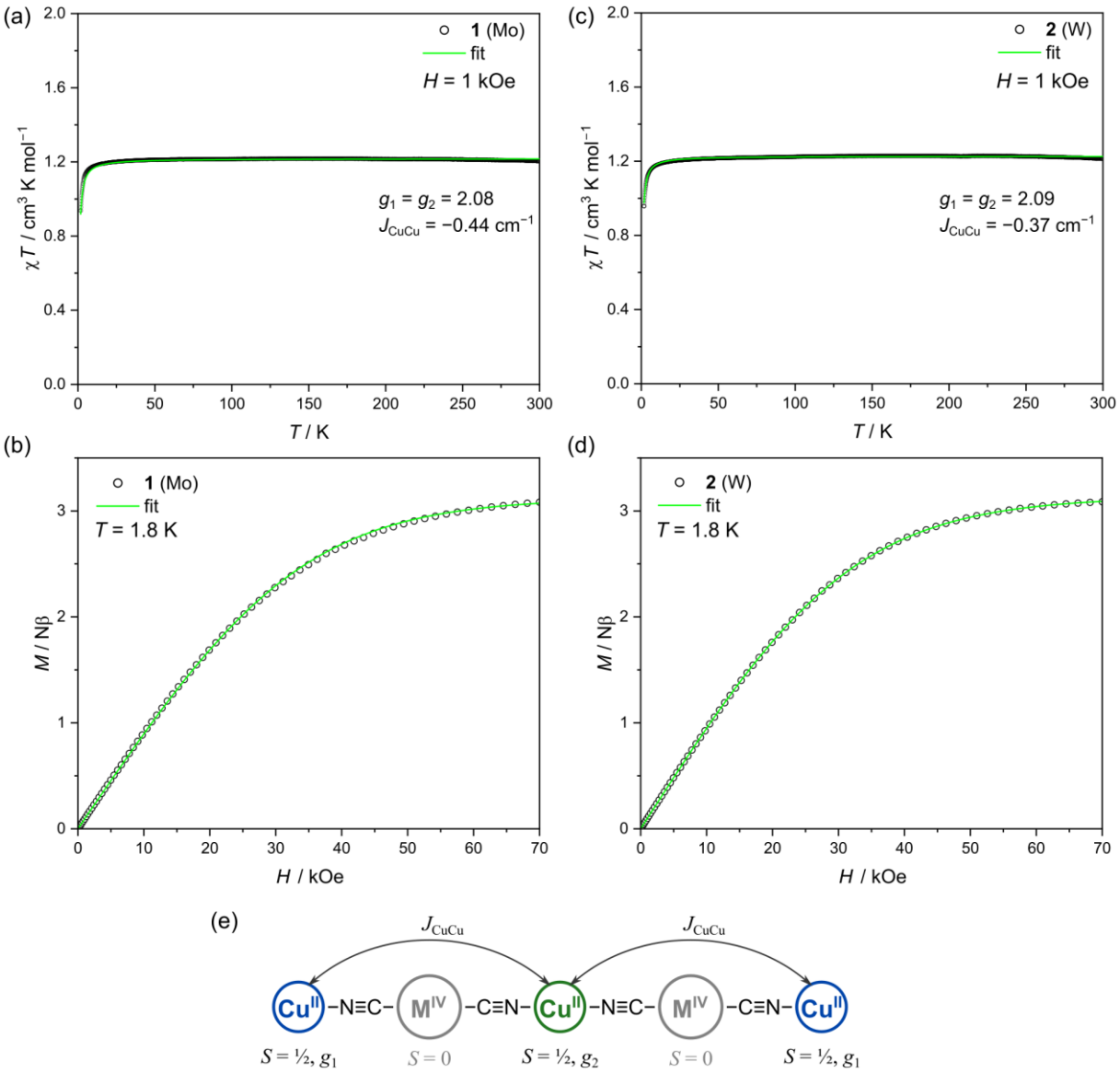

Figure S15. The bulk $\chi T(T)$ and $M(H)$ dependences for **1** (a,b) and **2** (c,d). Green lines represent the result of a concomitant fit of $\chi T(T)$ and $M(H)$ in PHI software[22] with a simplified model of a linear molecule composed of three Cu^{II} cations separated with diamagnetic $[M^{IV}(CN)_8]^{4-}$ species (e). To avoid overparameterization of the fit, the *g* factors for inequivalent Cu centers were assumed to be equal ($g_1 = g_2$), and only the magnetic exchange between the adjacent Cu centers was taken into account (J_{CuCu}). The fitted parameters are given.

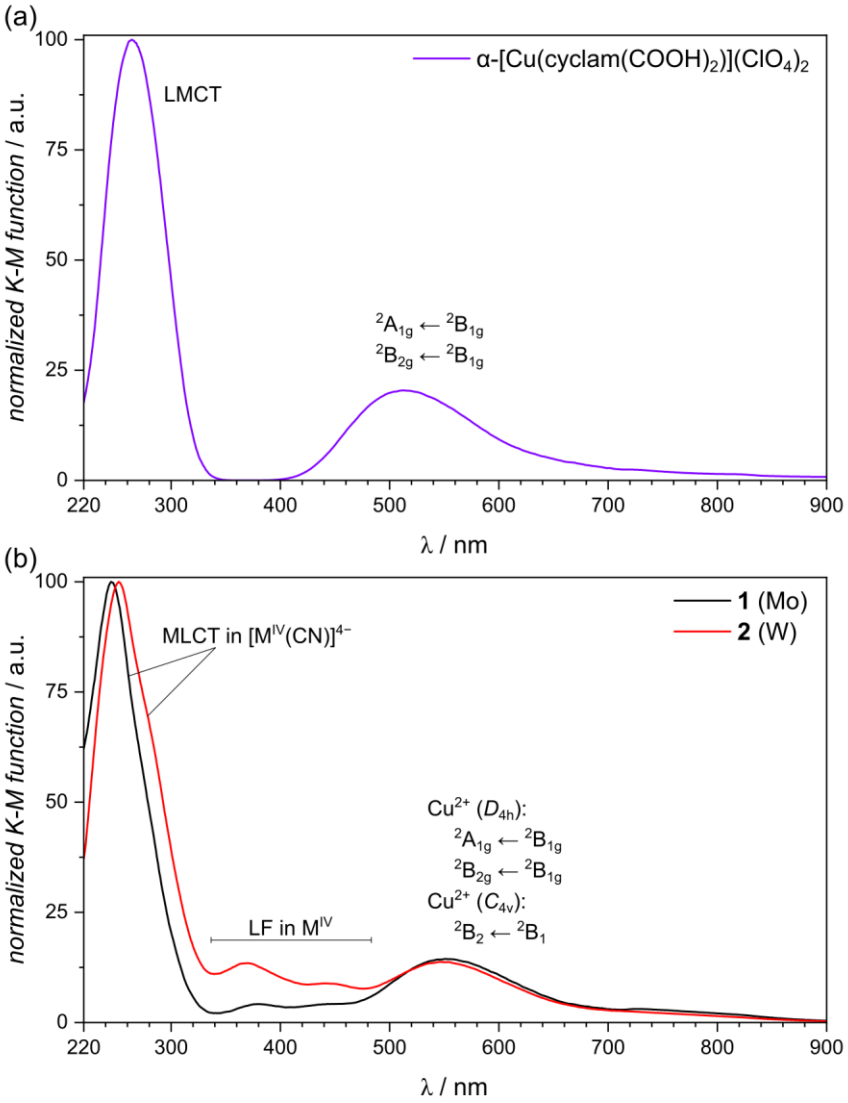

Figure S16. Comparison of diffuse reflectance spectra of (a) $[Cu(cyclam(COOH)_2)](ClO_4)_2$ and (b) compounds **1** and **2**.

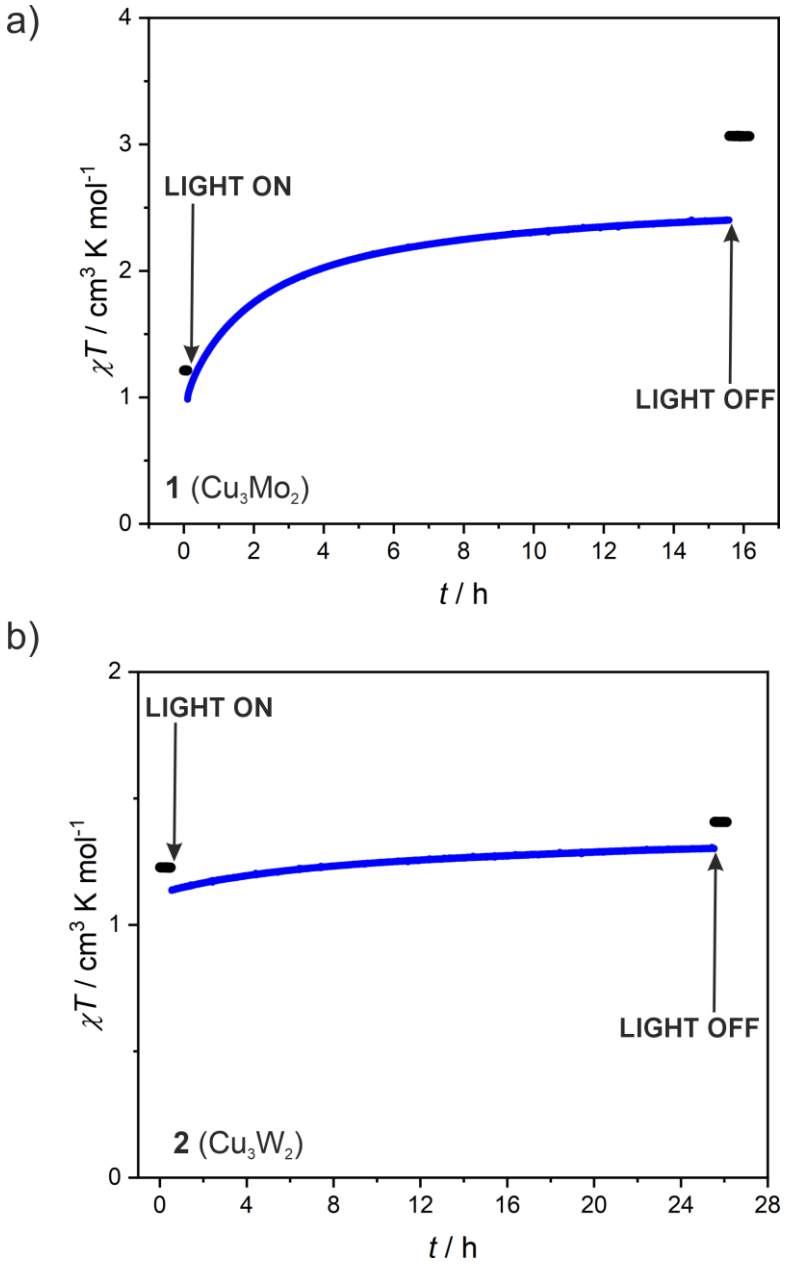

Figure S17. The $\chi T(t)$ dependences recorded during the 450 nm-light irradiation experiments at 10 K for **1** (a) and **2** (b) under H = 1 kOe. The black points represent the χT product in the absence of light.

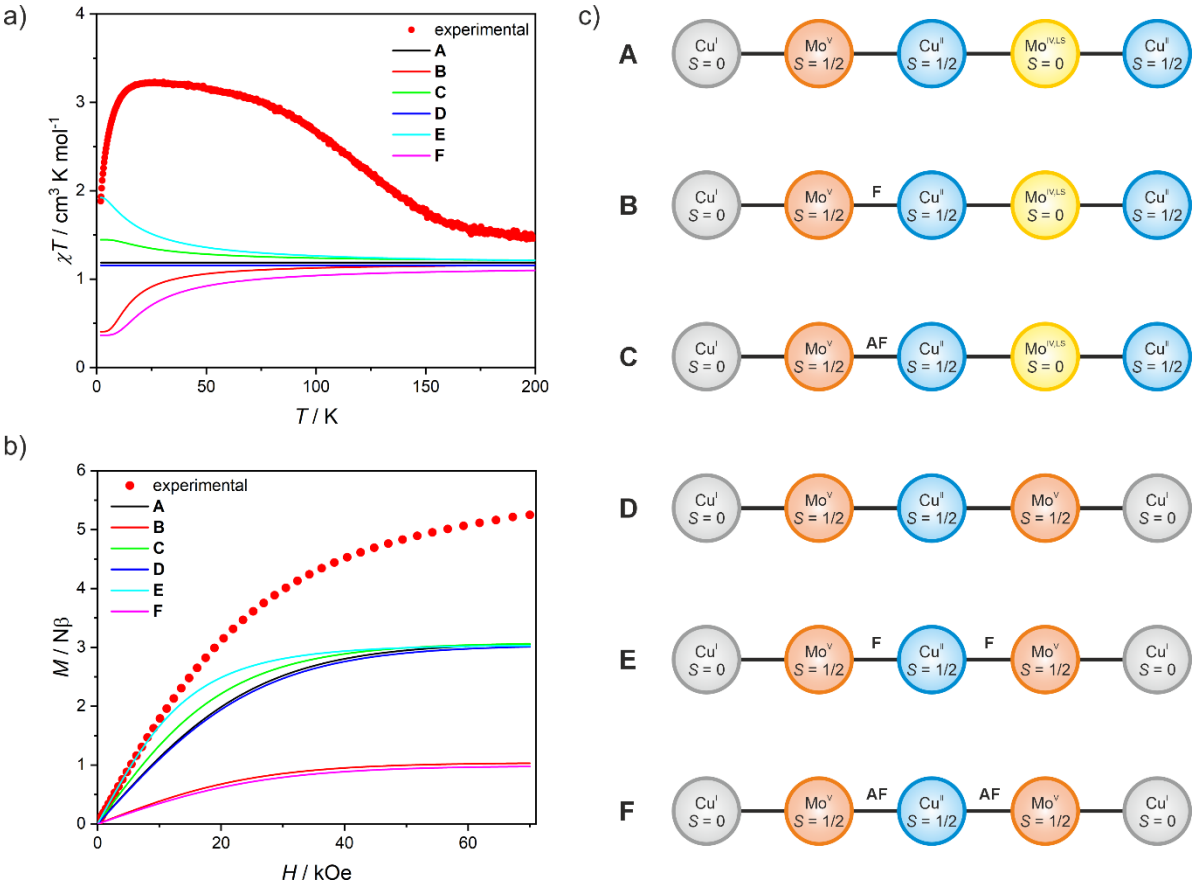

Figure S18. Experimental $\chi T(T)$ dependence at 1 kOe (a, red points) and $M(H)$ dependence at 1.8 K (b, red points) for **1** after photoirradiation, along with simulated magnetic properties (solid lines) for various MMCT scenarios (c); legend: F = ferromagnetic superexchange (J = +10 cm^{-1}), AF = antiferromagnetic superexchange (J = −10 cm^{-1}), g_{Cu} = 2.08, g_{Mo} = 2.00.

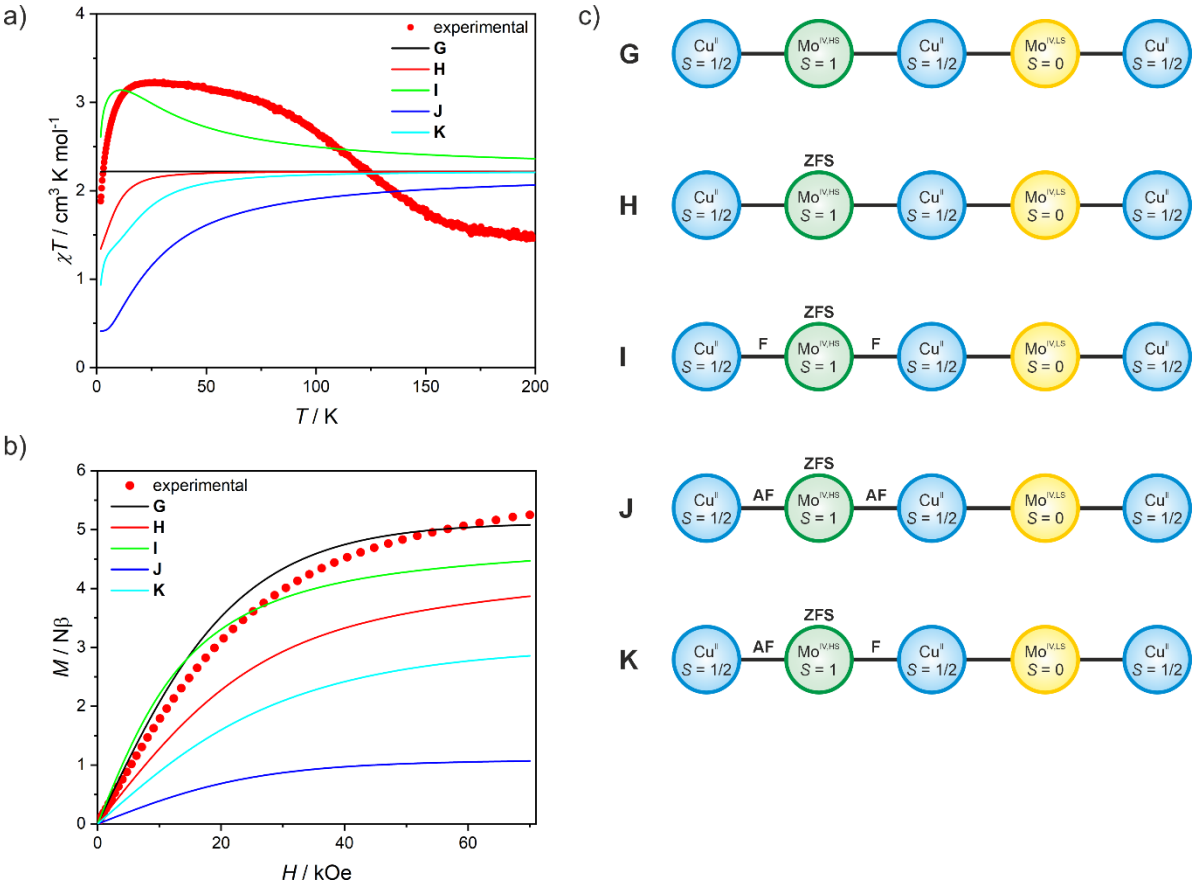

Figure S19. Experimental $\chi T(T)$ dependence at 1 kOe (a, red points) and $M(H)$ dependence at 1.8 K (b, red points) for **1** after photoirradiation, along with simulated magnetic properties (solid lines) for various LIESST scenarios assuming photoconversion of a single Mo center (c); legend: F = ferromagnetic superexchange (J = +10 cm^{-1}), AF = antiferromagnetic superexchange (J = −10 cm^{-1}), ZFS = zero-field splitting (D = +20 cm^{-1}), g_{Cu} = 2.08, g_{Mo} = 2.00.

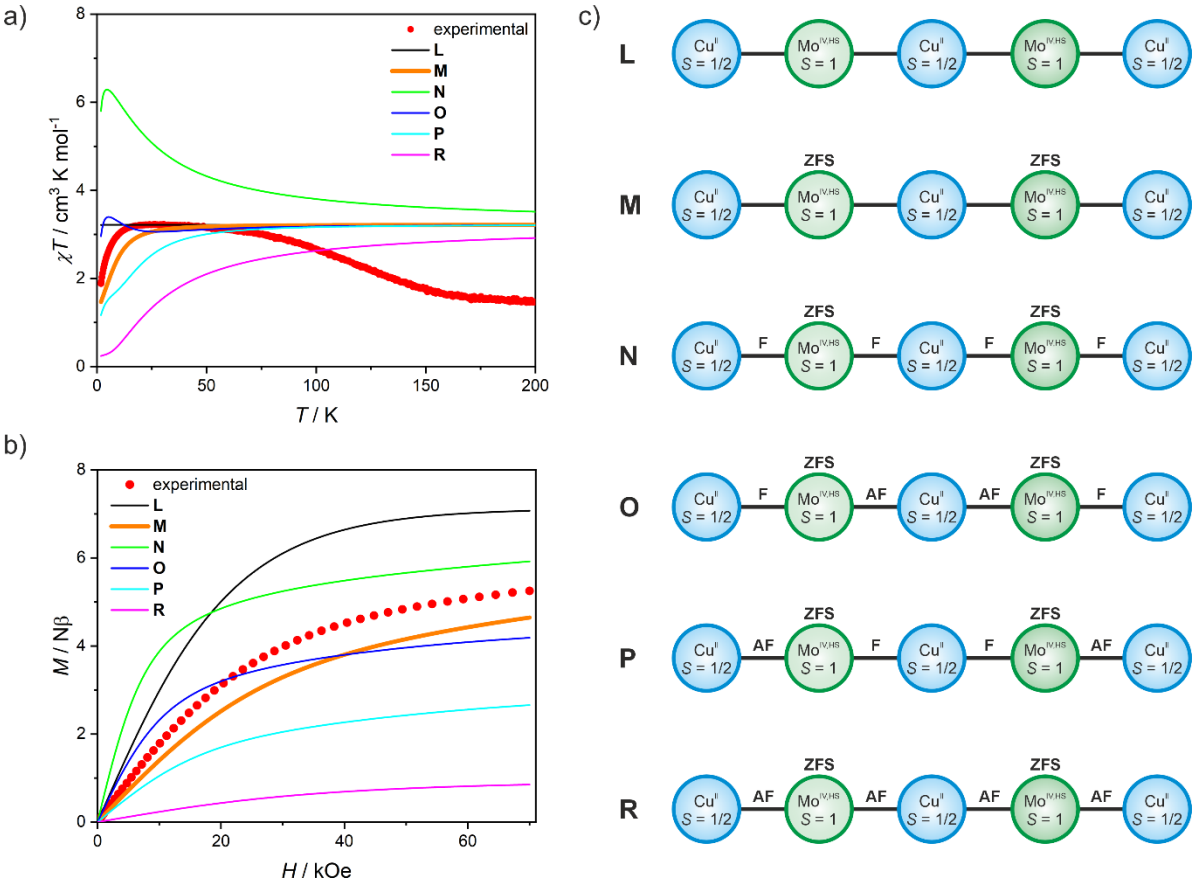

Figure S20. Experimental $\chi T(T)$ dependence at 1 kOe (a, red points) and $M(H)$ dependence at 1.8 K (b, red points) for **1** after photoirradiation, along with simulated magnetic properties (solid lines) for various LIESST scenarios assuming complete photoconversion of both Mo centers (c); legend: F = ferromagnetic superexchange (J = +10 cm^{-1}), AF = antiferromagnetic superexchange (J = −10 cm^{-1}), ZFS = zero-field splitting (D = +20 cm^{-1}), g_{Cu} = 2.08, g_{Mo} = 2.00.

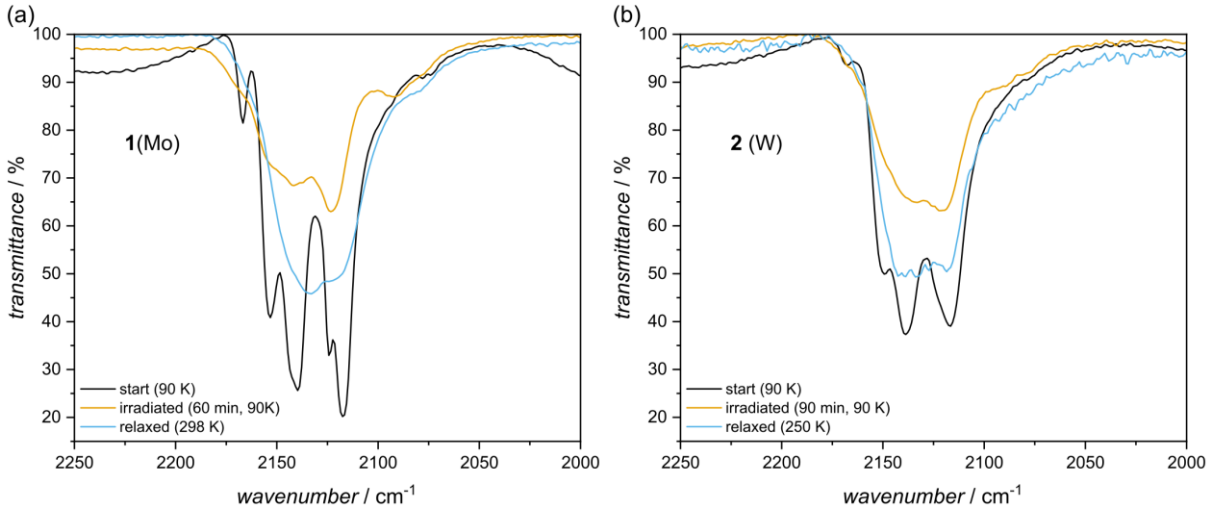

Figure S21. Changes in the FTIR spectra in the ν(CN) band range in **1** (a) and **2** (b) upon irradiation with 450 nm light at 90 K and after thermal relaxation.

References

1. L. Xin, N. F. Curtis and D. C. Weatherburn, Compounds of copper(II) and nickel(II) with 6,6,13,13-tetracarboxy-(and *E*-6,13-dicarboxy-) substituted 1,4,8,11-tetrazacyclotetradecanes, and carbomethoxy- and carbethoxy- derivatives. Structures of two isomeric *E*-6,13-dicarboxy- (and an *E*-6,13-dicarbomethoxy-)1,4,8,11-tetrazacyclotetradecane copper(II) perchlorates, *Transition Met. Chem.*, 1992, **17**, 147-154.
2. J. Zhu, P. M. Usov, W. Xu, P. J. Celis-Salazar, S. Lin, M. C. Kessinger, C. Landaverde-Alvarado, M. Cai, A. M. May, C. Slebodnick, D. Zhu, S. D. Senanayake and A. J. Morris, A New Class of Metal-Cyclam-Based Zirconium Metal–Organic Frameworks for CO_2 Adsorption and Chemical Fixation, *J. Am. Chem. Soc.*, 2018, **140**, 993-1003.
3. G. Handzlik, M. Magott, B. Sieklucka and D. Pinkowicz, Alternative Synthetic Route to Potassium Octacyanidoniobate(IV) and Its Molybdenum Congener, *Eur. J. Inorg. Chem.*, 2016, **2016**, 4872-4877.
4. D. Matoga, J. Szklarzewicz and M. Mikuriya, $[PPh_4]_3[W(CN)_7(O_2)]\cdot 4H_2O$ as the Representative of the $[M(L)_7(LL)]$ Class for Nine-Coordinate Complexes, *Inorg. Chem.*, 2006, **45**, 7100-7104.
5. N. F. Curtis, L. Xin and D. C. Weatherburn, Compounds of iron(III) with trans-1,4,8,11-tetraazacyclotetradecane-6,13-dicarboxylic acid: structures of trans-(trans-1,4,8,11-tetraazacyclotetradecane-6,13-dicarboxylato)iron(III) perchlorate and trans-(trans-1,4,8,11-tetraazacyclotetradecane-6,13-dicarboxylato)iron(III) trans-(trans-1,4,8,11-tetraazacyclotetradecane-6,13-dicarboxylic acid) dichloroiron(III) trans-1,4,8,11-tetraazoniacyclotetradecane-6,13-dicarboxylic acid dichloride tetraperchlorate tetrahydrate, *Inorg. Chem.*, 1993, **32**, 5838-5843.
6. M. Reczyński, M. Pazera and M. Magott, Proton Conductivity in Photomagnetic Cu^{II}_2-$[M^{IV}(CN)_8]$ Frameworks (M = Mo^{IV} and W^{IV}) Facilitated by the Tetracarboxy-Derivative of Cyclam, *Inorg. Chem.*, 2025, **64**, 7397-7406.
7. G. Sheldrick, SHELXT - Integrated space-group and crystal-structure determination, *Acta Crystallogr. A*, 2015, **71**, 3-8.
8. G. Sheldrick, A short history of SHELX, *Acta Crystallogr. A*, 2008, **64**, 112-122.
9. A. Altomare, C. Cuocci, C. Giacovazzo, A. Moliterni, R. Rizzi, N. Corriero and A. Falcicchio, EXPO2013: a kit of tools for phasing crystal structures from powder data, *J. Appl. Cryst.*, 2013, **46**, 1231-1235.
10. C. R. Groom, I. J. Bruno, M. P. Lightfoot and S. C. Ward, The Cambridge Structural Database, *Acta Crystallogr B Struct Sci Cryst Eng Mater*, 2016, **72**, 171-179.
11. J. Harrowfield, J. Y. Kim, Y. Kim, Y. H. Lee, Sujandi and P. Thuéry, Podand hexamines and the synthesis of pendent-arm tetra-azamacrocycles, *Polyhedron*, 2005, **24**, 968-975.
12. J. M. Harrowfield, Y. Kim, G. A. Koutsantonis, Y. H. Lee and P. Thuéry, Stereochemistry in Functionalized Macrocycle Complexes: Control of Hydroxyl Substituent Orientation, *Inorg. Chem.*, 2004, **43**, 1689-1696.
13. E. Samoľová, J. Kuchár, V. Grzimek, A. Kliuikov and E. Čižmár, Synthesis, crystal structure and magnetic properties of the new Cu(II)/Mn(II) coordination polymer $[\{Cu(cyclam)MnCl_3(H_2O)_2\}Cl]_n$, *Polyhedron*, 2019, **170**, 51-59.
14. E. Samoľová, J. Kuchár, E. Čižmár and M. Dušek, New heterobimetallic Cu(II)/Mn(II) complexes with trans-1,8-cyclam derivatives: Synthesis, characterization, magnetic properties and crystal structures of (μ_2-Chloro)-(dpc)-copper(II)-trichloro-manganese(II) and two polymorphs of (μ_2-Chloro)-(dac)-copper(II)-trichloro-manganese(II), *J. Mol. Struct.*, 2021, **1241**, 130592.
15. Z. Kotková, F. Koucký, J. Kotek, I. Císařová, D. Parker and P. Hermann, Copper(II) complexes of cyclams with N-(2,2,2-trifluoroethyl)-aminoalkyl pendant arms as potential probes for ^{19}F magnetic resonance imaging, *Dalton Trans.*, 2023, **52**, 1861-1875.
16. M. Lachkar, I. Halime, A. Bezgour, B. El Bali, M. Dusek, K. Fejfarova, S. Siddiq, B. P. Marasini, S. Noreen, A. Khan, S. Rasheed and M. I. Choudhary, Two new halocuprates complexes $[Cu^{II}$(1,4,8,11-tetraazacyclotetradecane)$][CuICl_3]$ and $[H_4$(1,4,8,11-tetrazacyclotetradecane)$][Cu_2ICl_6]$: synthesis, characterizations and biological studies, *Medicinal Chemistry Research*, 2012, **21**, 4290-4300.
17. C. S. F. W. Heinemann, R. Alsfasser, CCDC 2144413: Experimental Crystal Structure Determination. 2022, DOI: 10.5517/ccdc.csd.cc29zfmc.

18. L. Xue, Y. Li, X. Liu, Q. Liu, J. Shang, H. Duan, L. Dai and J. Shui, Zigzag carbon as efficient and stable oxygen reduction electrocatalyst for proton exchange membrane fuel cells, *Nat. Commun.*, 2018, **9**, 3819.
19. Y. H. Lee, M. Kim, A. R. Woo, J. Y. Choi, J. C. Byun, J. M. Harrowfield, W. T. Lim, P. Thuéry and Y. Kim, Small-ring heterocycles as components of multidentate ligands: some structural studies relating to ring opening, *Journal of Inclusion Phenomena and Macrocyclic Chemistry*, 2011, **71**, 395-407.
20. Y. H. Lau, J. K. Clegg, J. R. Price, R. B. Macquart, M. H. Todd and P. J. Rutledge, Molecular Switches for any pH: A Systematic Study of the Versatile Coordination Behaviour of Cyclam Scorpionands, *Chem. Eur. J.*, 2018, **24**, 1573-1585.
21. J. Pickardt and I. Hoffmeister, Crystal Structures of Two Copper(II) Cyclam Complexes: $[\{CuCl(C_{10}N_4H_{24})\}_2][CdCl_4]$ and $[Cu(C_{10}N_4H_{24})][CdCl_3(H_2O)_2]Cl$, *Z. Naturforsch. B*, 1995, **50**, 828-832.
22. N. F. Chilton, R. P. Anderson, L. D. Turner, A. Soncini and K. S. Murray, PHI: A powerful new program for the analysis of anisotropic monomeric and exchange-coupled polynuclear d- and f-block complexes, *J. Comput. Chem.*, 2013, **34**, 1164-1175.